DE GRUYTER High Temp. Mater. Proc. 2016; 35(7): 643–651

A. Muthuchamy, A. Raja Annamalai* and Rishabh Ranka

Mechanical and Electrochemical Characterization of Super-Solidus Sintered Austenitic Stainless Steel (316L)

DOI 10.1515/htmp-2015-0083
Received April 8, 2015; accepted June 23, 2015

Abstract: The present study compares the mechanical and electrochemical behaviour of austenitic (AISI 316L) stainless steel compacted at various pressures (200, 400 and 600 MPa) and conventionally sintered at super-solidus temperature of 1,400°C. The electrochemical behaviour was investigated in 0.1 N H_2SO_4 solution by potentiodynamic polarization and electrochemical impedance spectroscopy (EIS). The shrinkage decreased and densification has been increased with increasing pressure. The mechanical and electrochemical behaviour with pressure has been correlated with densification response and microstructure (pore type, volume and morphology). Highest densification (~92% theoretical) achieved at 600 MPa (compaction pressure) and 1,400°C (sintering temperature) resulted in excellent combination of tensile strength and ductility (456 ± 40 MPa, 25 ± 1.1%), while showing excellent corrosion resistance (0.1 mmpy or 4.7 mpy).

Keywords: austenitic stainless steel, compaction pressure, sintering, densification, electrochemical

Introduction

Austenitic stainless steels (316L) have been widely used in a variety of product forms for architectural, biomedical, industrial and nuclear applications due to its excellent corrosion and oxidation resistance, good strength (tensile strength 500–600 MPa), excellent toughness (impact 125 J at –200°C to 220 J at 90°C) and fabrication properties [1, 2]. Powder metallurgical (P/M) processing offers the advantage of low-cost net shaping with high material utilization (95%), relatively low-temperature processing and a more refined and homogeneous microstructure [3]. P/M stainless steels consolidated through solid state sintering at relatively low temperatures suffer from poor mechanical and corrosion properties, which are attributed to their inherent porosity [4–9]. The activated sintering routes (with pure elements like Al, Cu, Sn, etc.) adopted by researchers resulted in limited improvement in densification, and further compacts showed significant swelling (because of transient nature of liquid phases) beyond certain amount of activator which resulted in secondary porosity [10]. Alternatively, addition of phosphides (10 wt%) and boron (0.4 wt%) to stainless steel resulted in 96% and 98% of theoretical density, but exhibited poor mechanical properties due to the presence of brittle phase at grain boundaries [11–13]. Stainless steel powders are typically fabricated through atomization, which results in a single-phase prealloyed structure. Such prealloyed powders are amenable to consolidation at higher temperatures through super-solidus liquid phase sintering (SLPS) involving heating the compacts between the solidus and the liquidus temperatures [14, 15]. The liquid forms inside the particles and spreads to the particle contacts, resulting in a capillary stress induced pore filling and increased diffusion kinetics thereby enhancing densification. Panda et al. [16] reported the onset of melt formation for the prealloyed 316L powder as 1,383°C based on differential scanning calorimetry results. Correspondingly, the super-solidus sintering was carried out at 1,400°C, and its beneficial effects on the sintering response, mechanical properties and corrosion through potentiodynamic polarization of straight 316L have been reported individually by various researchers at particular compaction pressure (600 MPa) [17–19]. The amount of porosity in the final product has to be decided based on application and can be controlled by varying compaction pressures or sintering temperatures. Generally high compaction pressures are desirable as they give better dimensional control, less sintering shrinkage and higher final properties. The present work investigates the effect of compaction pressure on shrinkage, densification response, mechanical and

---

***Corresponding author: A. Raja Annamalai,** Manufacturing Division, SMBS, VIT University, Vellore 632014, Tamil Nadu, India, E-mail: raja.anna@gmail.com
A. Muthuchamy, Department of Metallurgical and Materials Engineering, Indian Institute of Technology Madras, Chennai 600036, India
Rishabh Ranka, Manufacturing Division, SMBS, VIT University, Vellore 632014, Tamil Nadu, India

electrochemical properties of austenitic stainless steel (AISI 316L) using tensile and bending (transverse rupture strength, TRS) tests, potentiodynamic polarization and electrochemical impedance spectroscopy (EIS).

Experimental procedure

The prealloyed water atomized 316L stainless steel powder; composition (wt%): Fe-16.5Cr-12.9Ni-2.48Mo-0.93Si-0.21Mn-0.025C-0.008S-0.01P); and average particle size ~50 μm was supplied by Krish Met, Chennai. Table 1 shown the Characteristics of as-received powders used in the present study. The powders were uniaxially compacted at three pressures (200, 400 and 600 MPa) to cylindrical pellets (~8 g, ~16 mm dia, ~5.8–7 mm thickness) using a hydraulic press using zinc stearate as a die wall lubricant. Sintering was carried out in hydrogen atmosphere (dew point: –35°C) in a $MoSi_2$-heated horizontal tubular sintering furnace (supplier: VB Ceramic Consultants, Chennai, India) at a constant heating rate of 5°C/min. The compacts were consolidated isothermally at 1,400°C for 1 h. Two intermediate isothermal holds of 15 min each at 600°C and 900°C were provided to ensure uniform temperature distribution, delubrication/debinding and reduction of oxides, respectively. The green and sintered densities were determined from dimensional (thickness and diameter) and weight measurements. The sinterability of compacts was determined through densification parameter, which is expressed as [1]

$$\text{Densification Parameter} = \frac{(\text{sintered density} - \text{green density})}{(\text{theoretical density} - \text{green density})} \tag{1}$$

The samples were polished to mirror finish and were ultrasonically cleaned in acetone for microstructural and electrochemical analyses. The microstructures of the samples were captured using an optical microscope (model: T1600, supplier: Metsonic Engineers, Secunderabad, India). Unetched metallographic samples were utilized to evaluate stereological parameters of the pore structure. Pore surface area and circumference measurement were accomplished with a Q-nodules image analysis system. For each sample, pore structure quantification was done on 10 micrographs captured randomly on top and sectioned surface. Marble's reagent (50 ml HCl and 25 ml saturated aqueous copper (II) sulphate) was used as etching agent. Bulk hardness of the samples was measured on Rockwell B scale (Leco V-100-C1 Hardness Tester). The microhardness of the samples was measured using Vickers' hardness tester at 0.1 kg load. The mechanical properties (yield strength, ultimate tensile strength, % elongation and TRS) were measured using flat tensile bars and transverse rupture bars pressed as per MPIF standards [20] with gauge length 26 mm using universal testing machine (INSTRON, UK) of full-load 20 kN at an initial strain rate of $3.3 \times 10^{-4}\ s^{-1}$ (crosshead speed 0.5 mm min^{-1}). The TRS of the sample was calculated as follows [1]:

$$\text{TRS} = \frac{3PL}{2t^2w} \tag{2}$$

where TRS = transverse rupture strength (N mm^{-2}), P = load to rupture (N), L = distance between the supporting rods, (26 mm), t = thickness of the specimen (mm) and w = width of the specimen (mm). To correlate the tensile properties with the microstructure, fractographs of the tensile tested samples were obtained using scanning electron microscopic (SEM) secondary electron imaging mode (Zeiss Evo 50, Carl Zeiss SMT Ltd., UK).

The electrochemical behaviour of the samples was studied in freely aerated 0.1 N H_2SO_4 solution (pH 1.31 ± 0.05) at room temperature using electrochemical system (model: IVIUM, supplier: Ivium Technologies, The Netherlands). Prior to polarization, the polished samples were allowed to stabilize for 3,600 s in 0.1 N H_2SO_4 to obtain stable open circuit potential (OCP). Electrochemical tests were carried out in a flat corrosion cell (supplier: Accutrol Inc., USA) using a standard three-electrode configuration with platinum mesh as the counterelectrode, Ag/AgCl (saturated with KCl) as reference electrode (+197 mV w.r.t hydrogen electrode) and the sample as the working electrode. Potentiodynamic polarization tests were carried out from –250 mV versus OCP to +1,600 mV versus reference electrode at a scan rate of 0.1667 mV s^{-1}. The corrosion potential (E_{corr}) and corrosion current (I_{corr}), corrosion rate, passivation current density (I_{pass}), critical current density (I_{crit}) and breakdown potential (E_b) were determined from

Table 1: Characteristics of the as-received powders used in the present study.

Property	Powder 316L
Powder shape - spherical	
Cummulative size, μm	
D_{10}	11.8
D_{50}	50.6
D_{90}	97.4
Specific surface area (m^2/g)	0.24
Theoretical density, g/cm^3	8

the polarization curves. EIS measurements were performed at room temperature after 1 h exposure (stabilization) in test solution (0.1 N H_2SO_4) to obtain stable OCP. EIS measurements were carried out at OCP with amplitude of 10 mV AC potential in the frequency range of 10^6–1 Hz. The equivalent circuit fitting was obtained using ZSimpWin software. During fitting, highest frequency points (between 10^6 and 10^5) were not been taken into consideration because they clearly corresponded to noise caused by the nonstabilities of the system.

Results and discussion

Densification studies

The densification responses of conventionally sintered samples are shown in Table 2. All the samples underwent shrinkage which decreased as compaction pressure increases. Increase in compaction pressure (from 200 to 600 MPa) resulted in ~40% decrease in radial shrinkage and ~60% decrease in axial shrinkage. In all samples the radial shrinkage is more than that of longitudinal or axial shrinkage. This can be attributed to the fact that during compaction, the pores get elongated and become ellipsoid shape with its long axis perpendicular to the pressing direction. The curvature associated with the longitudinal axis tends to get round in shape, which results in greater radial shrinkage as compared to the axial shrinkage. Figure 1 reveals the change in porosity shape during sintering. Densification parameter is the ratio of reduction in porosity during sintering to initial porosity after compaction as per eq. (1). The sintered density and densification parameter increased with increase in compaction pressure. The higher dislocation density because of high residual strain in samples compacted at high pressure (600 MPa) contributes to an initially faster sintering rate and correspondingly resulted in higher densification [3].

Microstructural features

Optical micrographs of conventionally sintered samples are shown in Figure 2. The microstructures revealed the presence of isolated pores with larger interpore distance in samples compacted at higher pressure (600 MPa) and open connected pores at near-grain boundaries and few isolated pores in samples compacted at lower pressures (200 and 400 MPa). The breakaway of grain boundaries from pores is higher, leaving only isolated pores in samples compacted at higher pressure (600 MPa) and less in samples compacted at lower pressures (200 and 400 MPa), which resulted in around 30–33% isolated pores and 67–70% interconnected pores at boundaries. Pore shape factor is calculated from pore surface area (A), and its circumference in the plane of analysis (P), as follows [21]:

$$F = \frac{4\pi A}{P^2} \tag{3}$$

Table 2: Effect of compaction pressure on densification response of 316L stainless steel sintered at 1,400°C.

Compaction pressure (MPa)	Green density ($g\ cm^{-3}$)	Radial shrinkage (%)	Axial shrinkage (%)	Sintered density ($g\ cm^{-3}$) (% density)	Densification parameter
200	5.52 ± 0.06	7.26 ± 0.04	5.47 ± 0.09	6.71 ± 0.06 (83.84)	0.48 ± 0.01
400	6.21 ± 0.01	4.39 ± 0.01	3.84 ± 0.1	7.05 ± 0.01 (88.10)	0.47 ± 0.005
600	6.58 ± 0.03	4.23 ± 0.01	3.37 ± 0.06	7.33 ± 0.03 (91.62)	0.53 ± 0.01

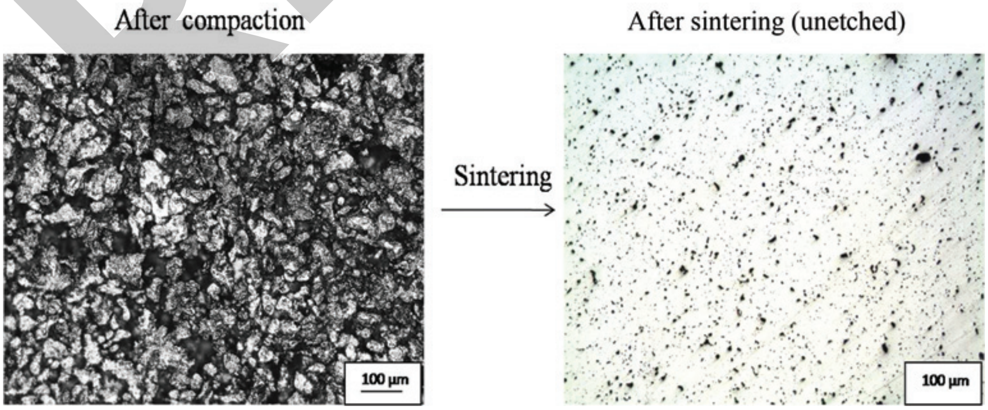

Figure 1: Schematic representation of the change in shape of porosity during sintering.

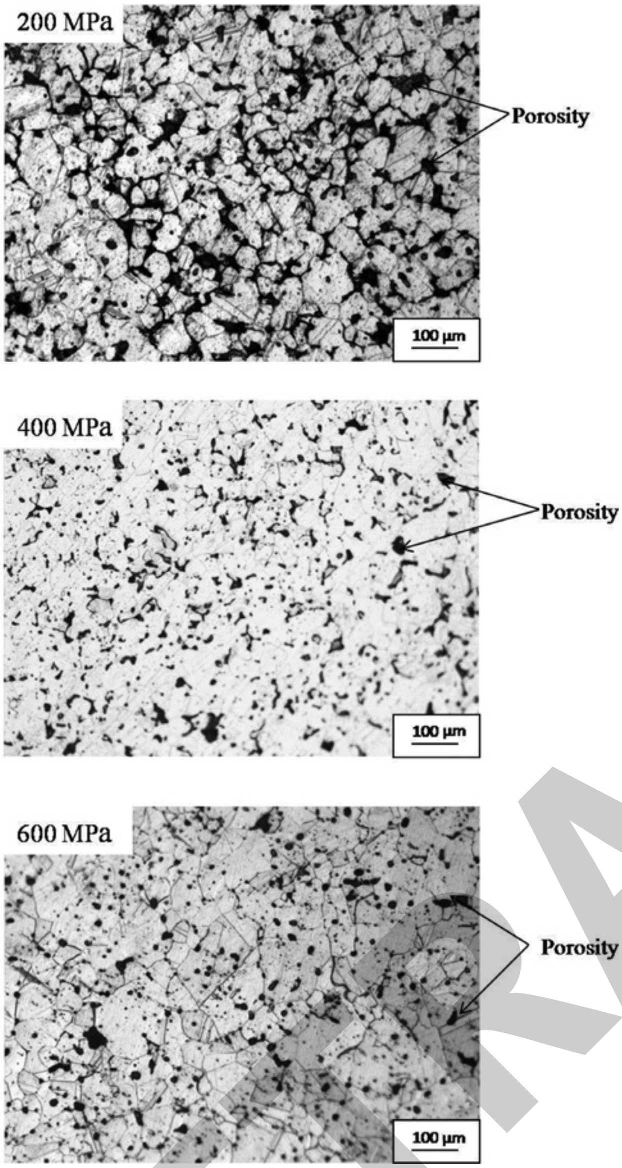

Figure 2: Optical micrographs of as-sintered 316L compacts and SEM micrographs of corroded samples compacted at different pressures (200, 400 and 600 MPa) and sintered at 1,400°C.

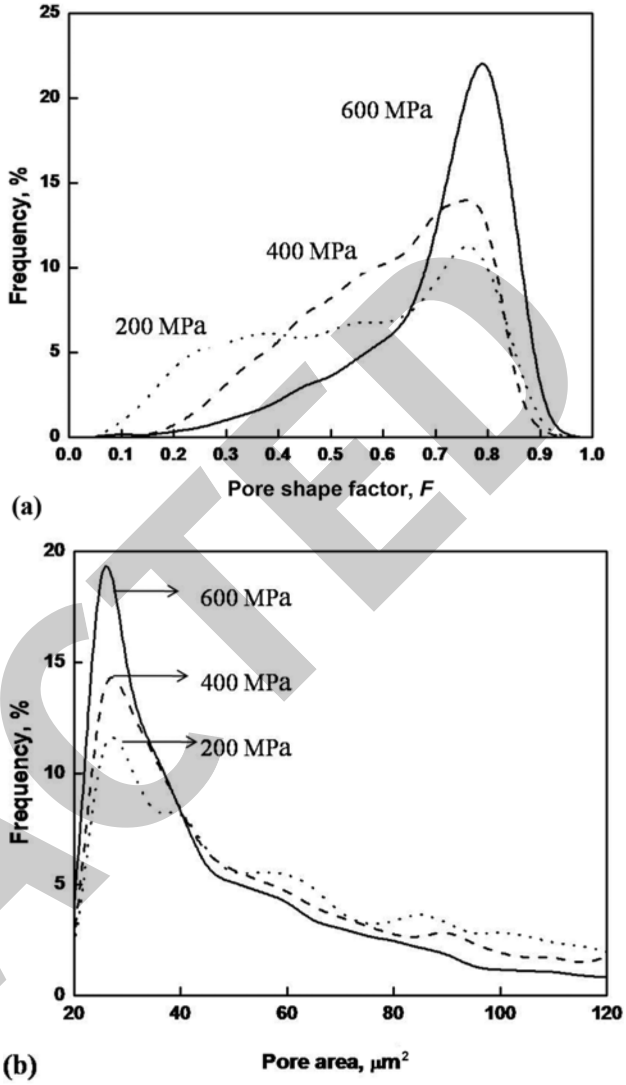

Figure 3: Comparison of (a) pore shape factor distribution and (b) pore area distribution of 316L samples compacted at different pressures (200, 400 and 600 MPa) and sintered at 1,400°C.

Pore shape factor (*F*) determines the profile irregularity of a pore. The shape factor of 1 represents a circular pore in the plane of analysis and as the number decreases from 1, the elongation and degree of irregularity increase. From the pore shape factor distribution in Figure 3(a), it can be observed that samples compacted at 600 MPa exhibited narrow distribution while others exhibited wide range of distribution. In all samples maximum frequency was obtained at shape factor close to 0.8. The frequency of rounded pores increased from ~11% to ~23% with increase in compaction pressure. Pore area distribution in Figure 3(b) revealed the presence of higher amount of fine pores (19%) in samples compacted at 600 MPa, while lesser amount of fine pores (~11% and 14%) in samples compacted at lower pressures (200 and 400 MPa).

Mechanical properties

Table 3 shows the effect of compaction pressure on the bulk and microhardness, strength and ductility of conventionally sintered 316L stainless steels. Stress–strain curves of as-sintered tensile samples are shown in Figure 4. Increase in compaction pressure from 200 to 600 MPa resulted in ~90–100% improvement in YS, UTS, % elongation and ~25% improvement in TRS, ~30% improvement in bulk hardness which can be directly

Table 3: Effect of compaction pressure on the mechanical properties of 316L stainless steel sintered at 1,400°C.

Compaction pressure (MPa)	Bulk hardness, HRB	Microhardness $HV_{0.1}$	Strength (MPa)			Elongation (%)
			YS	UTS	TRS	
200	47 ± 4	251 ± 44	135 ± 3	251 ± 15	818 ± 19	14 ± 0.2
400	55 ± 3	273 ± 37	182 ± 1	362 ± 7	912 ± 11	21 ± 0.8
600	61 ± 3	286 ± 30	224 ± 26	456 ± 40	1003 ± 15	25 ± 1.1

Note: YS, yield strength; UTS, ultimate tensile strength; TRS, transverse rupture strength.

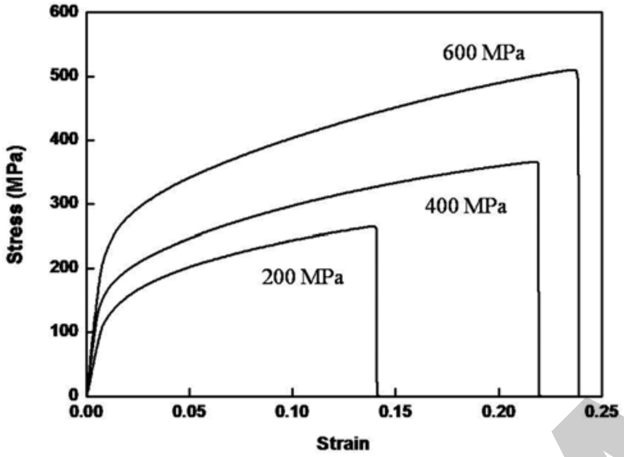

Figure 4: Stress–strain curves of the as-sintered tensile samples compacted at 200, 400 and 600 MPa and sintered at 1,400°C.

correlated to the higher sintered density (92% theoretical) and narrow pore shape factor and pore area distribution of samples. Samples compacted at 600 MPa resulted in excellent combination of tensile strength and % elongation (456 ± 40 MPa, 25 ± 1.1%) which are comparable to their cast products [22]. Microhardness increased with increase in pressure. The standard deviation is very high in all samples due to the presence of porosity and it is decreased with increase in pressure. In comparison to larger and closely spaced open pores present in samples compacted at lower pressures (200 and 400 MPa), small and largely placed isolated pores present in samples compacted at higher pressure (600 MPa) exhibited good mechanical properties. Poor strength values in case of samples compacted at 200 and 400 MPa can be attributed to higher pore volume (16% and 12%, respectively) and irregular pores (wide pore shape factor distribution), which resulted in poor load bearing capacity and more stress concentration. Poor work hardening, easy pore coalescence and crack initiation resulted in relatively lower ductility for samples compacted at low pressures (200 and 400 MPa) [3]. The fractographs depicted in Figure 5 revealed a cup and cone fracture for all samples which is indicative of rupture of material after a

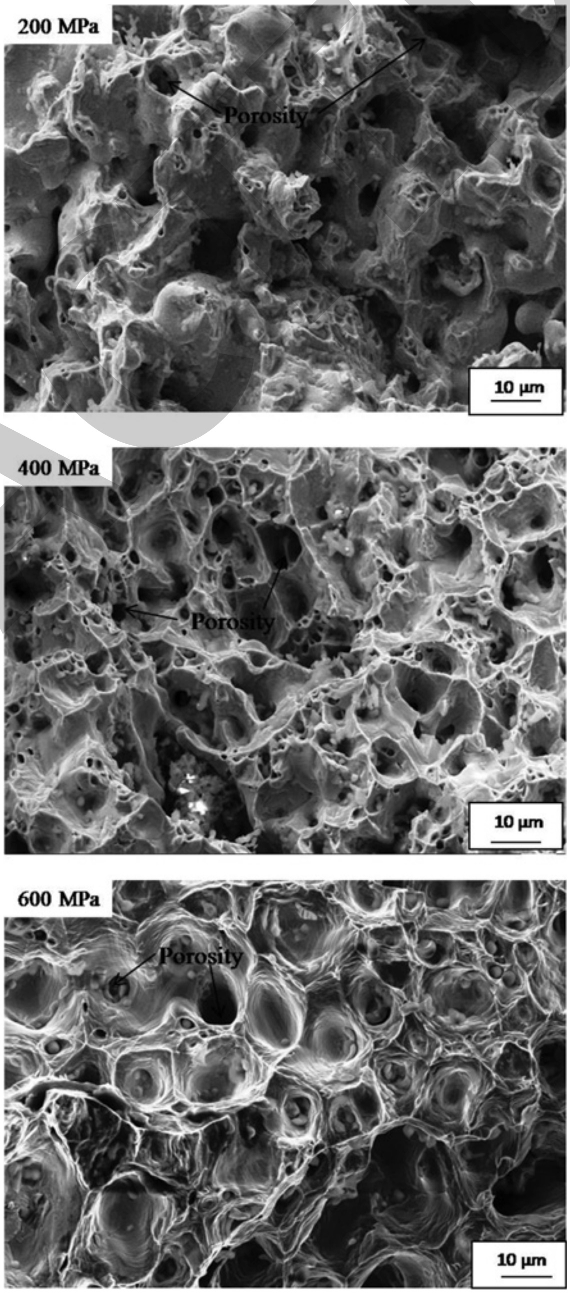

Figure 5: Fractographs of the as-sintered tensile samples compacted at various pressures (200, 400 and 600 MPa) and sintered at 1,400°C.

considerable amount of plastic deformation as a result of shear forces. The final shearing of the specimen produced a cup-type shape on one fracture surface and a cone shape on the adjacent connecting fracture surface. The presence of voids or cavities at matrix–pore interfaces indicates that the fracture nucleation, growth and crack propagation occurred at near pores.

Potentiodynamic polarization

The potentiodynamic polarization curves of samples compacted at different pressures and sintered at 1,400°C are shown as in Figure 6(a). All the samples exhibited typical active and passive transition behaviour followed by a trans-passive region typical of stainless steel [23]. A lower E_{corr} value (~267 mV) in case of 600 MPa samples is indicative of noble behaviour than others. Corrosion rate was calculated using the following expression [24]:

$$\text{Corrosionrate (mmpy)} = 3,268\frac{e}{\rho}I_{corr} \qquad (4)$$

where e is the equivalent weight (g), ρ the density of the material (g/cm^3) and I_{corr} the corrosion current (A cm^{-2}). The samples compacted at 600 MPa showed a much lower I_{crit} (6.38 μA cm^{-2}, two orders lower than samples compacted at 200 MPa) and I_{corr} value or corrosion rate (6.38 μA cm^{-2}, ~15 times lower than samples compacted at 200 MPa). Similar experimental results have been reported by various researchers [18, 19]. The critical current density (I_{crit}) provides insights on nucleation and growth of passive film and passivation current density (I_{pass}) assess the nature of the passive film formed. Lower the I_{crit}, the easier it is to passivate a material or to remain passive. A low I_{pass} implies slower diffusion of chromium through the passive film which is indicative of better corrosion resistance. Less pore volume (8%) and isolated porosity in case of samples compacted at 600 MPa lead to lower metal dissolution rate and better passivation behaviour with a low passivation current density (6.38 μA cm^{-2}). The presence of open porosity (surface) in case of samples compacted at lower pressures (200 and 400 MPa), corrosion rate is high due to easy diffusion of oxygen through pores and larger surface area exposure to corrosion electrolyte, while higher compaction pressure leads to reduced surface porosity and specific surface area, thus lessening interior corrosion through pore closure. The lesser corrosion rate is due to the more difficult diffusion of oxygen through the isolated pore structure [2]. From Figure 7, it can be clearly observed that localized corrosion at more number of triple junctions and along grain boundaries in case of samples compacted at lower pressures (200 and 400 MPa) while samples compacted at higher pressure (600 MPa) show substantially less number of triple junctions. The passive film broke nearly at the same potential for all the samples with the current densities approaching close values at substantially higher anodic potential (923 ± 11 mV). The presence of Mo (2.48 wt%) has restricted pitting as seen in Figure 7. In addition, lower concentration of electrolyte could also account for the absence of pitting (Table 4 & 5).

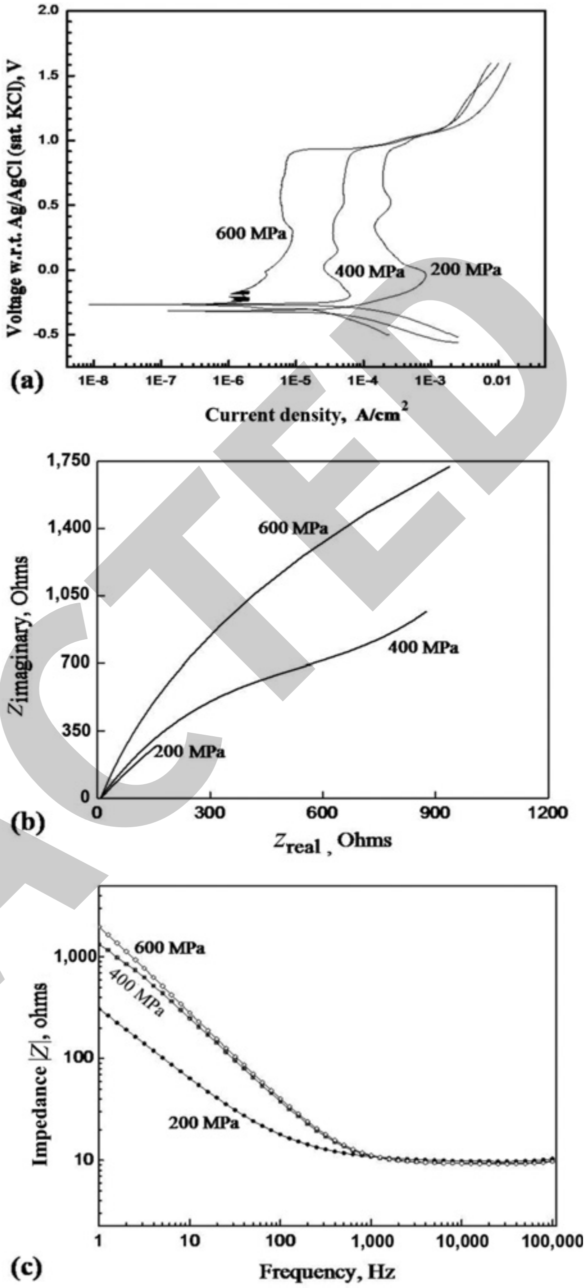

Figure 6: (a) Potentiodynamic polarization curves, (b) Nyquist plot and (c) Bode plot for 316L compacted at different pressures (200, 400 and 600 MPa) and sintered at 1,400°C.

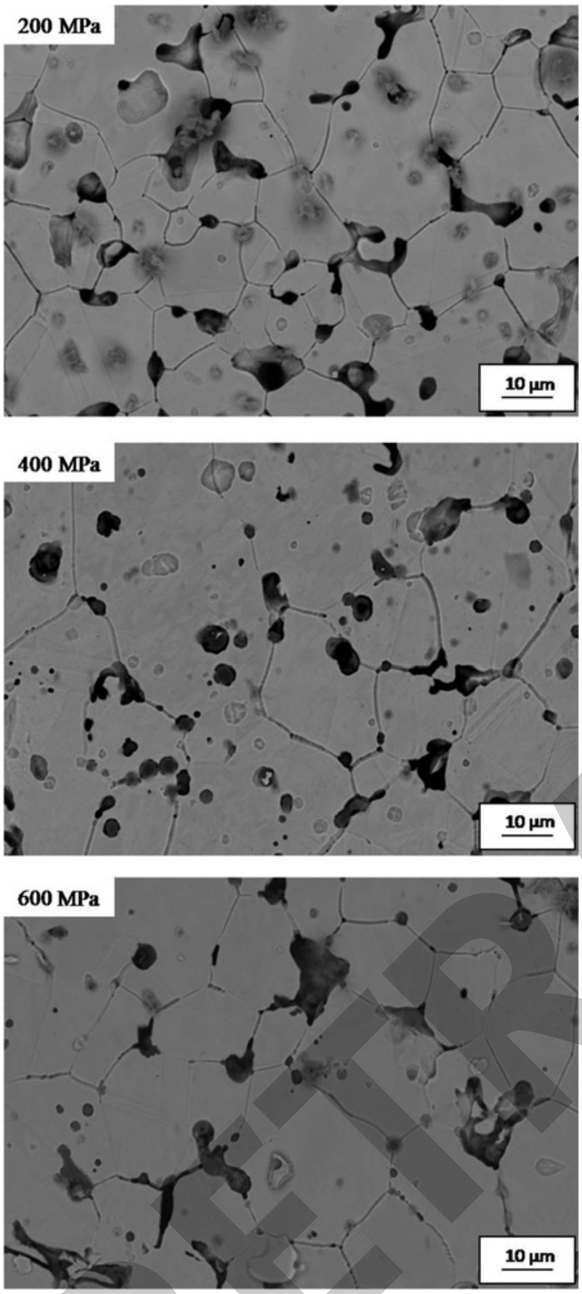

Figure 7: SEM micrographs of corroded 316L samples compacted at different pressures (200, 400 and 600 MPa) and sintered at 1,400°C.

Table 4: Effect of compaction pressure on the electrochemical behaviour of 316L compacts sintered at 1,400°C.

Compaction pressure (MPa)	E_{corr} (mV)	I_{crit} (µA cm^{-2})	I_{pass} (µA cm^{-2})	E_b (mV)	I_{corr} (µA cm^{-2})	Corrosion rate (mmpy)
200	−294	829	184	915	157	2.13
400	−269	65	36	918	45	0.58
600	−267	8.28	6.38	936	10	0.12

Table 5: Electrochemical impedance spectroscopy parameters obtained for 316L samples sintered at 1,400°C.

Compaction pressure	$R_{solution}$ (Ω cm^2)	CPE$_1$ (µF cm^{-2})	$R_{polarization}$ (Ω cm^2)	$C_{double\ layer}$ (µF cm^{-2})	$R_{charge\ transfer}$ (Ω cm^2)
200	10.46 (1.99%)	127.2 (5.65%)	48.54 (10.36%)	268.7 (5.98%)	527 (11.26%)
400	9.73 (1.82%)	40.76 (3.02%)	201.3 (11.88%)	42.7 (7.53%)	1,387 (6.7%)
600	9.61 (1.59%)	37.16 (2.78%)	211.7 (13.14%)	37.73 (6.03%)	3,421 (8.09%)

Note: Relative standard errors are mentioned in parenthesis.

Electrochemical impedance spectroscopy

The Nyquist plot and the Bode plot have been shown in Figure 6(b) and 6(c). After several attempts to simulate the EIS results with different circuits (two or three time constants in series, in parallel, etc.), the statistical study of the quality of the fittings and the possibility to assign a physical meaning to the components have led the authors to propose the circuit shown in Figure 8. The physical meaning of the components in the proposed circuit are (i) R_{ct} and C_{dl}, the resistance and capacitance associated with the charge transfer process that occur on the surface of the metal at low frequency; (ii) R_p and CPE$_1$, the resistance and the capacitance of the redox transformation of the corrosion products that occur on the surface of the oxide film at moderate frequency and (iii) the ohmic resistance of the solution (R_s) at higher frequencies. This circuit was used by few researchers to stimulate the electrochemical behaviour of passive materials such as stainless steels [25, 26] or titanium [27] in nonaggressive environments. Two time constants were not able to confirm directly from Bode or Nyquist plot because of the frequency range chosen in the present

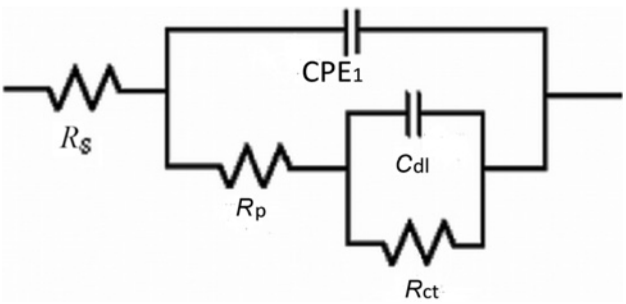

Figure 8: Equivalent circuit proposed to represent the corrosion mechanism of 316L samples compacted at three different pressures (200, 400 and 600 MPa) and sintered at 1,400°C.

study, i.e. 10^6–1 Hz, other researchers reported two maxima in Bode or Nyquist plot when the frequency range is 10^5–10^{-4} Hz. The values of the parameters obtained with the fitting procedure are reported in Table 5. The equivalent circuit with two time constants in series (**R(CR)(CR)**) used by G. Blanco et al. [28] gave slightly higher errors in our case. The capacitance CPE_1 and capacitance of double layer (C_{dl}) decreased with increase in compaction pressure. The obtained C_{dl} values in Table 5 are too high than typical capacitance corresponding to a charge transfer process. This can be due to the fact that pores make the real surface exposed to corrosion higher than that directly measured (apparent surface area). Similar results have been reported by other authors when the studied materials have surfaces with pores [29, 30]. The active area factor (AAF) proposed by A. Bautista et al. [24] can be used to estimate the real area that suffers the attack in P/M steels using EIS data. The AAF is calculated by dividing the experimental C_{dl} (Table 5) by 10 μF cm^{-2}. The calculated AAF values range between 4 and 27, which are comparable with those assumed by Fedrizz L. et al. [9], who considered that the active area may be 10–100 times the geometrical area, depending on the open porosity and pore shape. AAF decreases as the compaction pressure increases and it is closely related to the volume of the porosity of samples. The values obtained for polarization resistance (R_p) from the EIS spectra are about 1 order of magnitude lower than those obtained for charge transfer resistance (R_{ct}). Polarization resistance (R_p) is useful to estimate the ion release of an alloy in certain environment. Higher the R_p, the lower the ion release, subsequently lower corrosion rate. Higher the charge transfer resistance (R_{ct}), higher the protective ability of passive layer and low ion transfer rate and hence results in higher corrosion resistance. Larger diameter corresponding to samples compacted at higher pressure (600 MPa) in Nyquist plot shows higher polarization resistance (~4 times more compared to 200 MPa) and charge transfer resistance (~6 times more compared to 200 MPa) leading to lower metal dissolution and more passive behaviour than the samples compacted at lower pressures (200 and 400 MPa) due to less pore volume (8%) and absence of surface or interconnected pores.

Conclusion

In summary, all the samples underwent shrinkage which decreased as compaction pressure increases. In all samples the radial shrinkage is more than that of longitudinal or axial shrinkage. Pore volume, interpore spacing, morphology (shape and size) and nature (open or isolated) greatly affected the mechanical properties (strength, ductility and hardness) and kinetics of corrosion. The samples compacted at 600 MPa and sintered at 1,400°C (super-solidus) showed highest densification (92% of theoretical density), which correspondingly resulted in excellent combination of strength and ductility (456 ± 40 MPa, 25 ± 1.1%) and higher hardness (64 HRB) attributed to substantially less pore volume (8%) and rounded pores and excellent corrosion resistance (corrosion rate 0.12 mmpy or 4.7 mpy) due to the absence of interconnected pores in the sintered samples.

References

[1] R. M. German, Powder Metallurgy of Iron and Steel, John Wiley, New York (1998), pp. 437–460.

[2] E. Klar and P. Samal, Powder Metallurgy Stainless Steel, ASM International, Materials Park, OH (2007), p. 1.

[3] R. M. German, Powder Metallurgy Science Second Edition, Metal Powder Industries Federation, Princeton, NJ (1994), p. 21.

[4] P. K. Samal, J. B. Terrell and E. Klar, Effect of Sintering Atmosphere on the Corrosion Resistance and Mechanical Properties of Stainless Steels, Part II, MPIF, Princeton, NJ (2001), pp. 7–111 to 7–120.

[5] H. I. Sanderow and T. Prucher, Mechanical Properties of PM Stainless Steel: Advances in Powder Metallurgy and Particulate Materials, ed. M. Phillips, J. Porter, Vol. 3, Part 10, MPIF, Princeton, NJ (1995), pp. 10–13 to 10–28.

[6] J. A. Reinshagen and T. J. Brockius, Stainless steel based P/M alloys with improved corrosion resistance, in Advances in Powder Metallurgy and Particulate Materials, edited by M. Phillips and J. Porter, Vol. 3, MPIF, Princeton, NJ (1995), pp. 11–19 to 11–30.

[7] E. Otero, A. Pardo, M. V. Utrilla, E. Saenz and F. J. Alvarez, Corros. Sci., 40 (1998) 1421–1434.

[8] E. Otero, A. Pardo, M. V. Utrilla, E. Saenz and M. P. Hierro, Corros. Sci., 38 (1996) 1485–1493.

[9] L. Fedrizzi, J. Crousier, P. L. Bonora and J. P. Crousier Werkst. Korros., 42 (1991) 403–409.

[10] E. Deflorian, L. Ciaghi and J. Kozior Werkst. Korros., 43 (1992) 447.

[11] H. Preusse and J. D. Bolton, Powder Metall., 42 (1999) 51.

[12] A. Molinari, J. Kazior, F. Marchetti, R. Canteri, I. Cristofolini and A. Tiziani, Powder Metall., 37 (1994) 115.

[13] R. Tandon, Y. Liu and R. M. German, High density processing of ferrous alloys via super-solidus liquid phase sintering, in Advances in Powder Metal Particulate Materials, MPIF, Princeton, NJ, USA, 2 (1995), 5.23.

[14] R. M. German, Metall. Mater. Trans. A, 28A (1997) 1553–1567.

[15] L. Cambal, J. A. Lund Int. J. Powder Metall., 8 (1972) 131

[16] S. S. Panda, V. Singh, A. Upadhyaya and D. Agrawal Metall. Mater. Trans. A, 37 (2006) 2253.

[17] S. S. Panda, V. Singh, A. Upadhyaya and D. Agrawal, Scripta Mater., 54 (2006) 2179–2183.

[18] S. Balaji, P. Vijay and A. Upadhyaya, Scripta Mater., 56 (2007) 1063–1066.
[19] C. Padmavathi, A. Upadhyaya and D. Agrawal, Scripta Mater., 57 (2007) 651–654.
[20] MPIF Standard 10, Tension test specimens for pressed and sintered metal powders, MPIF Standard 41: Determination of transverse rupture strength of sintered metal powder test specimen", Standard test methods for Metal Powders and Powder Metallurgy Products, Metal Powder Industries Federation, Princeton, NJ, USA, 1991.
[21] Metallography: An Introduction, Metallography and Microstructures, Vol. 9. ASM Handbook ASM International (2004), 1017.
[22] Properties and Selection: Irons, Steels, and High-Performance Alloys, Vol. 1. ASM Handbook ASM International (1990), 1326.
[23] A. J. Sedriks, Corrosion, 42 (1986) 376–388.
[24] E. Bardal, Corrosion and Protection, Springer-Verlag, London (2004), p. 9.
[25] C. R.Clayton and I. Olefjord Passivity of Austenitic Stainless Steels. In Corrosion Mechanism Theory and Practice, edited by P. Marcus, J. Oudar, Marcel Dekker, New York (1995), pp. 175–199.
[26] C. M. Abreu, M. J. Cristobal, R. Losada, X. R. Novoa, G. Pena and M. C. Perez, J. Electro Anal. Chem., 572 (2004) 335–345.
[27] J. Pan, C. Leygraf, D. Thierry and A. M. Ektessabi, J. Biomater. Res., 35 (1997) 309–318.
[28] G. Blanco, A. Bautista and H. Takenouti, Cement Concrete Comp., 28 (2006) 212–219.
[29] A. V. C Sobral, W. Ristow Jr, D. S. Azambuja, I. Costa and C. V. Franco, Corros. Sci., 43 (2001) 1019–1030.
[30] A. Bautista, A. González-Centeno, G. Blanco and S. Guzmán, Mater. Charact., 59 (2008) 32–39.